

# X-ray Texture Analysis and Imaging of Engineering Materials at Oxford HEX-lab

Alexander M. Korsunsky\*, Mengyin Xie, Nikolaos Baimpas and Xu Song

**Abstract** — At the High Energy X-ray laboratory (HEX-lab, Department of Engineering Science, University of Oxford, UK) we carry out studies of deformation and structure of engineering materials and components. Laboratory and synchrotron X-ray beams provide the principal means of analysis and measurement. A variety of other techniques are also in use. We present a range of applications and case studies in high performance engineering materials.

**Index Terms**— HEX-lab, synchrotron x-ray, texture, tomography

## I. INTRODUCTION

The characterization of the structure and deformation behavior of engineering materials plays a pivotal, underpinning role in the improvement of understanding of the property-performance relationship (together with micro-structural and micro-mechanical modeling, e.g. by FEM).

The research carried out at the High Energy X-ray laboratory (HEX-lab) in the Department of Engineering Science at Oxford utilizes mono- and poly-chromatic beams of energetic X-ray photons for the purposes of imaging, spectroscopic analysis and diffraction. Some of the studies are carried out using sealed X-ray tubes with Cu and W targets. Others make use of the environmental Scanning Electron Microscope (e-SEM) or optical imaging. Finally, range of experiments that require ultimate precision and spatial or temporal resolution are carried out at the nearby Harwell Oxford site. The Centre for In situ Processing Studies (CIPS) housed at the Research Complex at Harwell (RCaH) supports experiments at ISIS neutron and muon spallation source, and also at Diamond Light Source (DLS) synchrotron facility. As frequently in the modern practice, only when a vast range of analytical tools is brought to bear upon individual problems

\* Manuscript received Dec 28, 2011; revised Feb 10, 2012.

Professor Alexander M. Korsunsky is with the Department of Engineering Science, University of Oxford, UK, OX1 3PJ (corresponding author, phone: +44-18652-73043; fax: +44-18652-73010; e-mail: [alexander.korsunsky@eng.ox.ac.uk](mailto:alexander.korsunsky@eng.ox.ac.uk)).

Mengyin Xie is doctoral student in the Department of Engineering Science, University of Oxford, UK, OX1 3PJ (e-mail: [mengyin.xie@eng.ox.ac.uk](mailto:mengyin.xie@eng.ox.ac.uk)).

Nikolaos Baimpas is doctoral student in the Department of Engineering Science, University of Oxford, UK, OX1 3PJ (e-mail: [nikolaos.baimpas@eng.ox.ac.uk](mailto:nikolaos.baimpas@eng.ox.ac.uk)).

Dr Xu Song was doctoral student and Research Associate with the University of Oxford, UK, OX1 3PJ, and is now with the Singapore Institute of Manufacturing Technology, A\* Star, Singapore, 638075 (e-mail: [songx02@gmail.com](mailto:songx02@gmail.com)).

may complementary characterization and multi-aspect view be achieved.

In this paper we present an overview of several recent studies of engineering materials.

## II. EVALUATION OF THE ORIENTATION DISTRIBUTION FUNCTION (ODF) BY SYNCHROTRON X-RAY DIFFRACTION

The preferred orientation (texture) of polycrystalline materials gives rise to anisotropy in its mechanical properties, such as the stress-strain relationship, yield surface and crack propagation. Texture in engineering components is usually introduced by plastic deformation during the manufacturing process, and is of significant interest for predicting component performance. This section describes the experiment and analysis procedures that allow the determination of the Orientation Distribution Function (ODF, the full mathematical description of texture, [1]) for a wire manufactured from tungsten, W (body-centred cubic crystal lattice) by extrusion. The use of synchrotron X-ray powder diffraction for data collection is described, and the prediction of the elastic anisotropy of the sample is made and discussed.

The experiment was conducted at beamline I12 (JEEP), Diamond Light Source, Didcot, UK. A monochromatic synchrotron X-ray beam at 80 keV and with a beam size of 1mm × 1mm was used to irradiate the tungsten wire. The schematic of the experimental setup is shown in Fig. 1a. The wire was mounted to parallel with Y axis and perpendicular to the incident X-ray beam (Z direction). The wire was rotated in 5° increment from -85° to +90° around the Y axis. Powder diffraction condition was achieved and Debye-Scherrer diffraction patterns were recorded after each rotation. Due to the preferred orientation of the grains, the Debye-Scherrer rings showed strong anisotropy (Fig. 1b). The ring pattern was binned into 5° angle sectors (“caked”, [2]) and integrated to obtain equivalent 2θ diffraction line profiles. A Matlab routine was used to perform single peak fitting and thus to determine the location of peak centers and the integrated peak intensity. After data processing, each diffraction peak was assigned three parameters: 1) 2θ, the peak center position on the equivalent 2θ diffraction line profile; 2) δ, the azimuthal angle on the Debye-Scherrer pattern; 3) ω, the rotation angle of the sample around Y axis. The data for integrated diffraction peak intensity as a function of these coordinates can be noted down as a discrete table of values of the continuous function  $I_{hkl}(2\theta, \delta, \omega)$ . The intensity function  $I_{hkl}(2\theta, \delta, \omega)$  is directly related to the probability of finding a specific  $hkl$  plane normal (pole) at certain spatial direction on a unit sphere covering all possible spatial directions [2, 3].

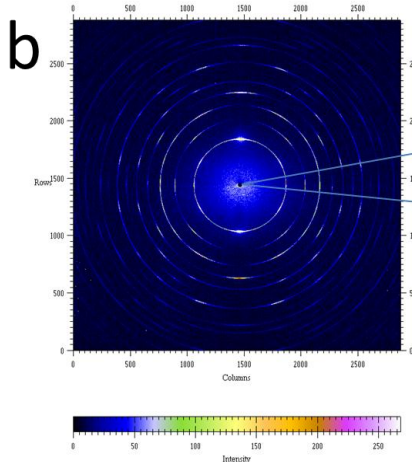
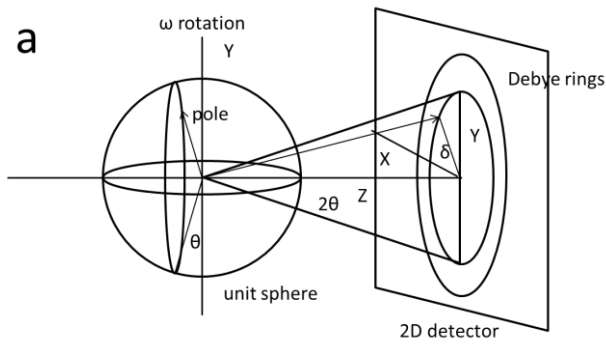


Fig. 1a). A schematic diagram of the experimental setup; b). Debye-Scherrer diffraction pattern for the tungsten wire.

To provide a visualization of the sample texture, the intensity values  $I_{hkl}(2\theta, \delta, \omega)$  need to be projected onto a plane. This projection for a specific  $hkl$  pole is called a pole figure. The following describes the process of transformation of intensity functions into pole figures. The method represents a modified version of Wenk's pioneering work [3].

Firstly, the intensity function  $I_{hkl}(2\theta, \delta, \omega)$  is converted to another intensity function  $P(a, b)$  (here,  $a$  and  $b$  are the longitude and latitude on the spherical surface respectively). If there is no rotation, the Cartesian coordinates of an  $hkl$  pole on the unit sphere are given by,

$$\mathbf{r}(\theta, \delta) = \begin{bmatrix} \cos \theta \cos \delta \\ \cos \theta \sin \delta \\ \sin \theta \end{bmatrix} \quad (1)$$

After rotation by an angle of  $\omega$  around Y axis, the vector is transformed into

$$\mathbf{r}'(\theta, \delta, \omega) = \mathbf{R}(\mathbf{Y}, \omega) \mathbf{r}(\theta, \delta) = \begin{bmatrix} \cos \omega & 0 & \sin \omega \\ 0 & 1 & 0 \\ -\sin \omega & 0 & \cos \omega \end{bmatrix} \begin{bmatrix} \cos \theta \cos \delta \\ \cos \theta \sin \delta \\ \sin \theta \end{bmatrix} \quad (2)$$

The longitude  $a$  and latitude  $b$  have the following relationship with  $\mathbf{r}'$ :

$$\tan a = \frac{r'(2)}{r'(1)} \quad (3)$$

$$\tan b = \frac{r'(3)}{\sqrt{r'(1)^2 + r'(2)^2}} \quad (4)$$

The next step is to project this new intensity function  $P(a, b)$  onto the sphere's equatorial plane using equal area projection. The relationship between the spherical coordinates and the two pole figure coordinates are,

$$\beta_E = \frac{L_E}{\sqrt{2}} \times 90^\circ = \sqrt{2} \sin \frac{(\pi/2 - b)}{2} \times 90^\circ \quad (5)$$

$$\alpha_E = a \quad (6)$$

The above procedures can be summarized as below,

$$I(2\theta, \delta, \omega) \xrightarrow{\text{transformation}} P(a, b) \xrightarrow{\text{projection}} P(\alpha_E, \beta_E)$$

The range of pole distance angle ( $\beta_E$ ) is  $[0, 90^\circ]$ , and the azimuthal angle ( $\alpha_E$ ) range is  $[-180^\circ, 180^\circ]$ . A grid with the cell's size of  $5^\circ \times 5^\circ$  is introduced, covering the entire pole figure. All intensity points that fall within a cell are summed up to represent the intensity of the cell. Fig. 2 shows the pole figures of (110), (200) and (211) poles of the sample obtained using the procedure described.

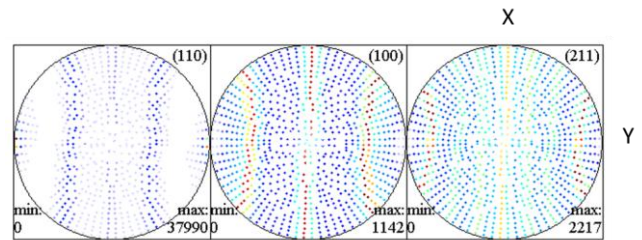


Fig. 2. raw pole figures of (110), (200) and (211) plane normal of the tungsten wire, the (100) pole figure is equivalent to (200) one. Here, X and Y refer to the projections of X and Y axis of in the lab coordinate system (wire axis horizontal). Z axis projection lies at the center of the pole figure.

If the value of the (110) pole intensity function was forced to unit (for example  $I_{110}(2\theta, \delta, \omega) = 1$ ), the pole figure for this specific case was shown in Fig. 3. It is called the coverage of (110) poles, showing that what poles have been covered by the experimental method. Fig. 3 tells that few spatial directions around Z axis in lab coordinates have been probed but the ones around Y axis have been measured more than once. This pole coverage is usually plotted before an experiment to check whether the planned rotation is enough to cover a least required number of poles for ODF calculation. The intensity in the pole figure is yet not uniform to one as was set for the intensity function ( $I_{110}(2\theta, \delta, \omega)$ ). Therefore, normalization has to be performed to all pole figures in Fig. 2 by dividing them with their unique coverage.

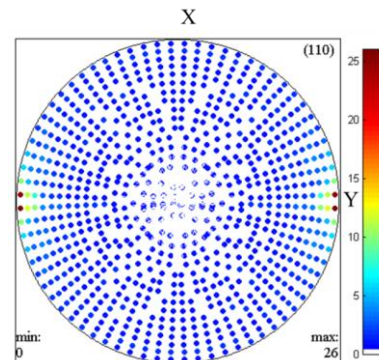


Fig. 3. (110) pole coverage

Apart from normalization, to speed up the determination of the orientation distribution function (ODF), blank regions in Fig. 3. are filled in by interpolation. The interpolation procedure is based on the assumption that the intensity variation around each circle (the locus of points of equal pole distance  $\beta$ ) can be expanded into a series over harmonic functions,

$$f(\alpha) = m_0 + m_1 \cos(2\alpha) + m_2 \cos(4\alpha) + \dots + m_i \cos(2i\alpha) \quad (7)$$

In the analysis procedure, each circle was first approximated by harmonic functions using least squares fitting, and the blank regions then filled by the predictions from the fitted functions. However, the central part of the pole figures remains too sparsely populated with data to fit. As a consequence, the central area had to be removed from the pole figures. The new pole figures are shown in Fig. 4., with the intensity plotted on the logarithmic scale.

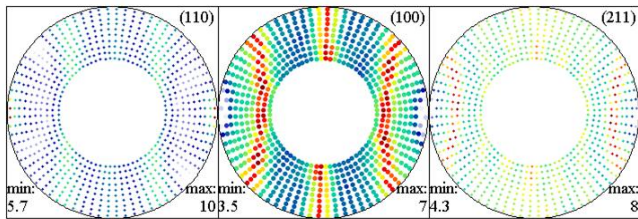


Fig 4. Pole figures after normalization and interpolation

The pole figures shown in Fig. 4. were used as input to calculate the full ODF. The MTEX toolbox combined with Matlab routines was used. The ODF was approximated by up to 100,000 radially symmetric unimodal bell functions [4]. Then a method similar to least square fitting was used to adjust the coefficients in order to achieve the smallest error between the calculated and experimentally collected pole figures. The ODF is the probability density function  $f(\varphi_1, \Phi, \varphi_2)$  of finding the crystal orientation specified by the three Euler angles  $\varphi_1, \Phi, \varphi_2$ . Bunge's definition of Euler angles was used in the present study [3]. The full pole figures reproduced by the calculated ODF are shown in the upper row of Fig. 5. The density distributions show good agreement with the results in Fig. 4. The absolute density is different due to the automatic normalization performed by MTEX.

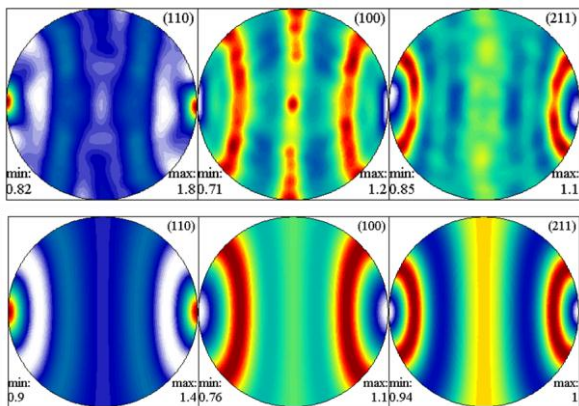


Fig. 5. Experimental (upper row) and simulated (lower row) pole figures. (Wire axis horizontal).

We now discuss the significance of these pole figures. In the lower row of Fig. 5, the three pole figures were plotted from the simulated ODF for fiber texture in a bcc metal. The similarity between the upper and lower row confirms that the

sample studied had a typical fiber texture. When polycrystalline aggregates experienced largely tensile plastic deformation, the closest-packed planes ( $\{110\}$  in bcc crystal) have the trend to align with the tensile direction in order to minimize the surface energy [4]. In this case, the Y axis corresponds to the extrusion direction and strong  $(110)$  pole distributions are found around the Y axis.

Based on the complete orientation ODF, the elastic modulus pole figure could also be computed. In the context of the scope of the present review, it is interesting to reference recent work that focused on the anisotropy of mechanical properties of human dentin, the building material for teeth [6]. The largest value of the Young's modulus is observed around the Y axis (Fig. 6), but the difference between the maximum and minimum value computed is relatively small. This is due to the fact that the Zener anisotropy factor of Tungsten is only about 1.01[7], i.e. differs from unity by only 1%. Thus for this material the anisotropy of elastic properties remains small even in the case of strong preferred orientation.

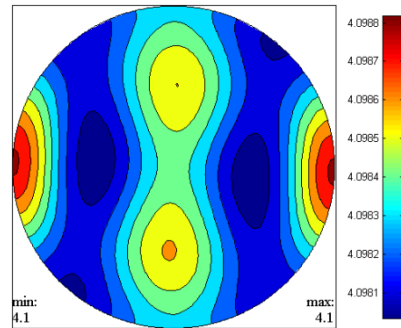


Fig. 6. Young's modulus pole figure

### III. LABORATORY AND SYNCHROTRON X-RAY TOMOGRAPHY AND DEFORMATION ANALYSIS

Three-dimensional X-ray imaging of the internal structure of materials and components provides unique insights into the relationships between structure and deformation response. X-ray tomography in particular has become one of the most widely used techniques for non-destructive cross-sectional imaging of an object from transmission data ("projections") collected by illuminating the object from many different directions [8]. At a given rotation angle ( $\varphi$ ), the measured value harvested by the detector is the transmitted intensity through the object,  $I(x)$ . Comparison of this intensity with the "flood field" value allows the calculation of the total absorption integral of the incident beam through the sample:

$$p(x, \varphi) = \ln(I_0 / I) = \int_{L(x, \varphi)} \mu \rho(x, y) dy \quad (8)$$

Here  $p(x, \varphi)$  denotes the element of data that corresponds to a particular pixel across the detector ( $x$ ) at a specific angle of rotation ( $\varphi$ ) and with  $\rho(x, y)$  being the (a priori unknown) 2D density distribution within the sample cross-section;  $y$  is the coordinate in the direction of beam propagation through the sample, with  $L(x, \varphi)$  being the path length; and  $\mu$  is the total mass attenuation coefficient:

$$\mu = \mu_{abs} + \mu_{coh} + \mu_{incoh} \quad (9)$$

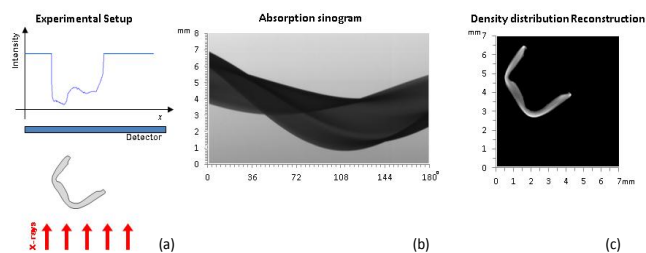


Fig. 7: Summary of steps taken to obtaining a tomographic reconstruction by absorption-contrast: (a) One of the measured intensity profiles; (b) The compounded absorption sinogram; (c) The 2D reconstruction of the density distribution (“slice”) (all data collected in the present project).

Thus total mass attenuation coefficient is the sum of the contributions of the photoelectric absorption, the coherent ( $\mu_{coh}$ - Rayleigh) and the incoherent ( $\mu_{incoh}$ - Compton) scattering. A convenient source of the numerical values of the absorption coefficients is, for example, the NIST database XCOM [9].

Fig. 7 illustrates the tomographic setup in the Oxford HEX-lab. Starting at the reference angle (denoted  $0^\circ$ ), “shadow” projections are collected of the 3D sample onto the 2D detector, as the sample is consecutively rotated, at constant rotation steps, around a vertical axis that is aligned to be parallel to the vertical column of pixels on the detector. Projections are repeatedly collected until the rotation angle of  $180^\circ$  is reached.

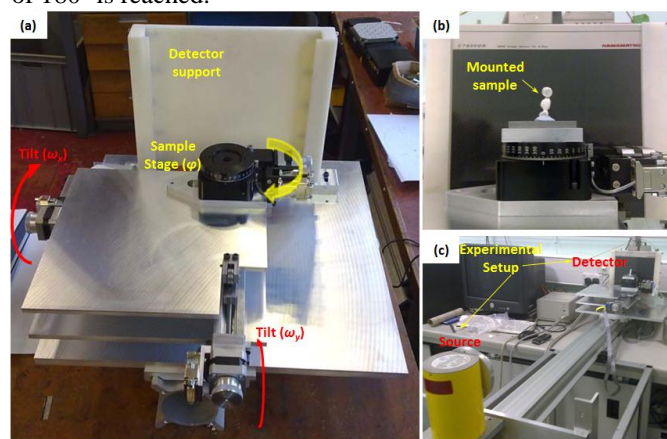


Fig. 8. a) Schematic illustration of HEX-lab tomographic setup; b) Fixed prosthetic denture (FPD) mounted in front of the Hamamatsu X-ray detector and c) general view of the setup.

In this setup, each horizontal row of pixels on the detector captures consecutively different angle line projections of the same sample slice perpendicular to the rotation axis. The entire slice dataset can be summarised in a compound 2D diagram (with axes representing rotation angle and position in the row) that is referred to as the “sinogram” (Fig. 7b). The sinogram provides the input required for common inversion algorithms (e.g. Filtered Back Projection (FBP) based on the inverse radon transform) that can solve the inverse problem. The key theoretical basis of tomographic back projection techniques is the Fourier Slice Theorem that relates the measured projection data to the two-dimensional Fourier transform of the object cross section [8].

In the HEX-lab X-ray radiography (tomography) setup (illustrated in Fig 8) located in the Department of Engineering Science, University of Oxford, we employ an Yxlon<sup>®</sup> industrial X-ray source (160kV, 2.25kW) and a Hamamatsu<sup>®</sup> X-ray detector. The black motorized rotation

stage for locating the sample at different projection angles  $\varphi$  with respect to the incident beam is placed in the centre, in front of the mounting frame for the X-ray detector. Fig. 8b shows a closer view of a fixed prosthetic denture (FPD) mounted in front of the X-ray detector (Hamamatsu<sup>®</sup>). Careful adjustment is required in terms of stage tilts in the vertical and horizontal planes. This is accomplished through the use of linear translation motorised stages seen at the front and on the left of the assembly (Fig 8a). The translation stages are coupled to the plate underneath the main rotation through small angle wedges, so that relatively large displacements on the translators result in relatively small changes in the stage tilts ( $\omega_x, \omega_y$ ). This allows tilt accuracies better than  $0.1^\circ$  to be achieved. Fig. 8c shows a general view of the setup highlighting the Cu source and the 2D detector used. Finally, translations of the entire assembly are also possible in the horizontal plane, along the beam direction and perpendicular to it.

The alternative, higher flux and higher resolution tomography setup used in this study was located at the synchrotron instrument JEEP (I12), the Joint Engineering, Environmental and Processing beamline at Diamond Light Source (DLS, Harwell Oxford, UK).

A dedicated hard X-ray parallel monochromatic beam setup is available with the energy range 50 - 150 keV and the

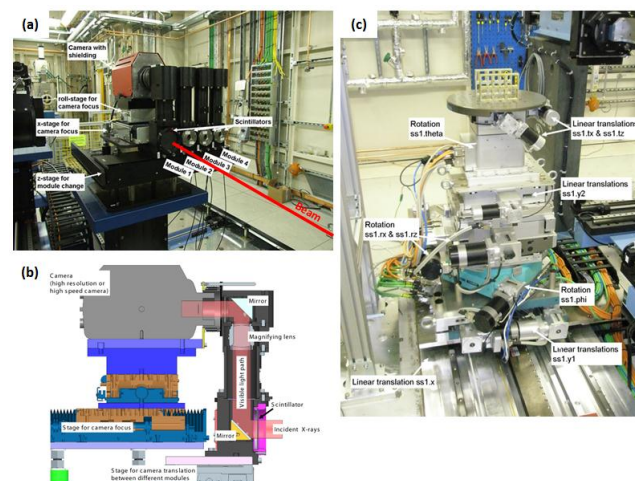


Fig. 9. a) Illustration of the mounted camera setup showing the different magnification modules; b) Schematic cross-section illustration of the PCO - scintillator interchangeable setup using two  $45^\circ$  mirrors; c) general view of the tomography setup with highlighted translations-rotations.

energy resolution is  $10^{-3}$ - $10^{-4}$ , depending on the Si monochromator setting. For high resolution tomography, a PCO 4000 camera is used with the  $4008 \times 2672$  pixel matrix, capable of the framing rate of 5fps (Fig. 9a-b). Four different scintillators and magnification optics (modules) are used to convert X-rays to visible light, giving great flexibility to the setup in terms of the resolution (pixel size) and field of view (Fig. 9a). The magnification and field of view settings vary from  $0.7 \times$  and  $48.8\text{mm} \times 32.2\text{mm}$  to  $10 \times$  and  $3.6 \text{mm} \times 2.4 \text{mm}$ . Fig. 9c shows, in front of the detector, the test setup that offers a range of 3D linear translations, rotation around the axis perpendicular to the beam and various tilting substages for alignment purposes.

Recent evolution of the available X-ray sources has allowed the application of tomography to various engineering problems. Using high resolution tomography along with novel techniques such as Digital Volume

Correlation techniques (DVC), it is possible to acquire quantitative information for the displacement fields by gradient estimation techniques and through them calculate strain fields, e.g. under the application of an external load [10].

Below we consider two examples of X-ray tomography and compare the results from HEX-lab portable source setup to those obtained from a dedicated hard monochromatic X-ray synchrotron beamline I12 at DLS.

Two tomography experiments using the same specimen were carried out in the HEX-lab and on I12. A sample with the approximate shape of 8mm diameter tube was composed of bonded hollow spheres of commercially pure (CP) Ni. Sphere diameters varied in the range 1-2mm, while their wall thickness was about 0.1 mm. In the HEX-lab, 180 projections were acquired by rotating the sample in steps of 1°. A divergent cone of white (polychromatic) beam was used. Due to the relatively large source to sample distance (>1500mm) and the small sample to detector (<200mm)

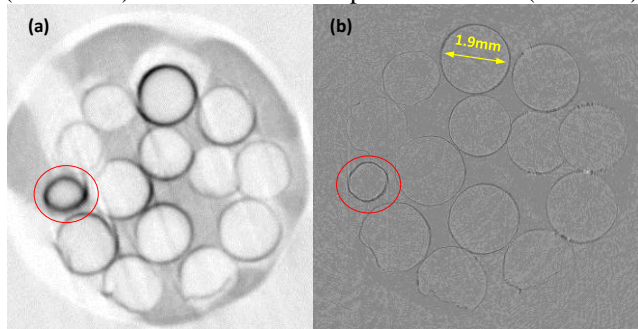


Fig. 10. Ni hollow spheres single cross-section reconstruction at approximately the same height (a) HEX-lab, (b) DLS I12.

distance, parallel beam interpretation strategy was employed. Exposure time of 1s was used for each projection. The 3D volume representation from the data was reconstructed using filtered back-projection algorithm (iradon) implemented in Matlab®. The resulting reconstruction was rendered by introducing an intensity threshold (Fig. 10). In the I12 (DLS) experiment, 900 projections were acquired by rotating the sample in steps of 0.9°. The parallel beam was monochromated to 53.4 keV. The exposure time for each projection was 1.58s, and Module 3 was used with the field of view 20.0×13.3mm and 5µm pixel size. The reconstructions were carried out using the software available at DLS beamline I12 (Manchester-Diamond package) using the filtered back projection reconstruction approach.

The second set of samples used in the experiments was an all-ceramic dental bridge framework (FPD) made from anatomically reduced bridge copings using Wieland ZENO® Zr sintered zirconia ceramic material (Wieland Dental + Technik, Pforzheim, Germany) and porcelain veneer in the case of the DLS experiment. In HEX-lab, 360 projections were acquired at 0.5° steps using a 1.5s exposure time for each projection. The 3D volume representation from the data was reconstructed using filtered back-projection algorithm (iradon) implemented in Matlab®. The resulting reconstruction was rendered by introducing an intensity threshold, with the result shown in Fig. 11. On beamline I12 at DLS, 1800 projections were acquired by rotating the sample in steps of 0.1°. Parallel monochromatic beam procedure was used, and a 1.64s exposure time was chosen to match the dynamic range of the detector.

Fig. 10 shows a single cross-section reconstruction from both HEX-lab and DLS setups. A significant difference in the dynamic range-contrast of the two reconstructions is directly noticeable, with the sphere structure being more clearly visible in the HEX-lab reconstruction. The relatively low absorption of the hard monochromatic X-rays in the synchrotron experiment may have an adverse effect on the

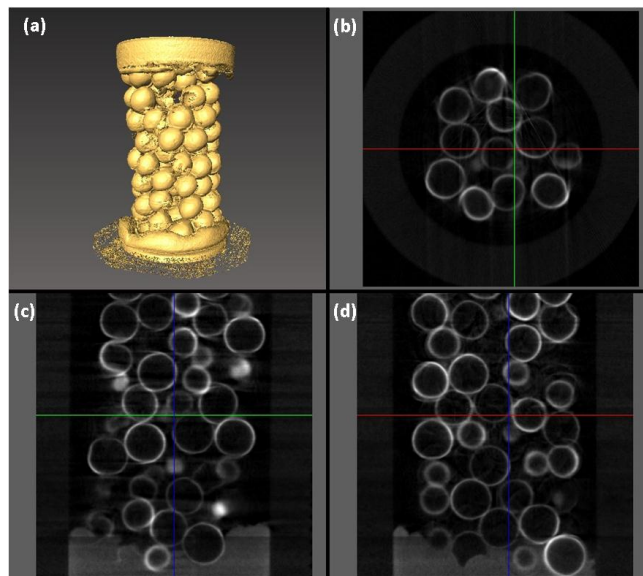


Fig. 11. Ni hollow spheres representation using Avizo® for HEX-lab data set. (a) 3D data rendering, (b) view x-y, (c) view y-z and (d) view x-z.

quality of the reconstruction, making rendering of the volume more challenging. 50keV represents the minimum energy threshold that can be achieved on I12, by design of the S1 monochromator. It is worth noting, however, that the cell wall shape is captured better in the DLS reconstructions. This is both due to the significantly larger number of projections (900), and the use of the 5µm pixel (module 3) compared to 180 projections in HEX-lab data, and the ~35µm pixel size of the Hamamatsu detector. This resolution difference also affects the apparent cell thickness of the spheres. Finally, we note that the cells highlighted by the red circles in Fig. 10a and 10b have irregular ellipsoidal shapes and display artefacts on their periphery. This phenomenon was also observed in some other spheres within the bulk, indicating that some of the cells may not have been properly attached to the rest of the assembly, thus moving during the rotation of the stage.

A pseudo-3D representation of the sample is shown in Fig. 11. This is a 3D volume rendering obtained by introducing a density threshold in AVISO® software for the visualisation of HEX-lab data for all slices. Figs. 11b, c and d are arbitrarily chosen orthogonal slices that are used for qualitative evaluation of the reconstruction data from Oxford HEX-lab. We note that due to the limited contrast in the DLS reconstruction data, an equivalent representation was not possible without using more complex routines, such as edge detection filtering.

Fig. 12a is a 3D volume representation of the uncoated Zirconia fixed prosthetic denture (FPD) sample on the basis of HEX-lab data. The high absorption of ZrO<sub>2</sub> in combination with using 360 projection angles gave a satisfactory reconstruction. The box illustrates the equivalent field of view of module 3 used in DLS, and the segmented section of the Zirconia part of a similar sample with porcelain coating, shown in Fig. 12b. Finally, Fig. 12c

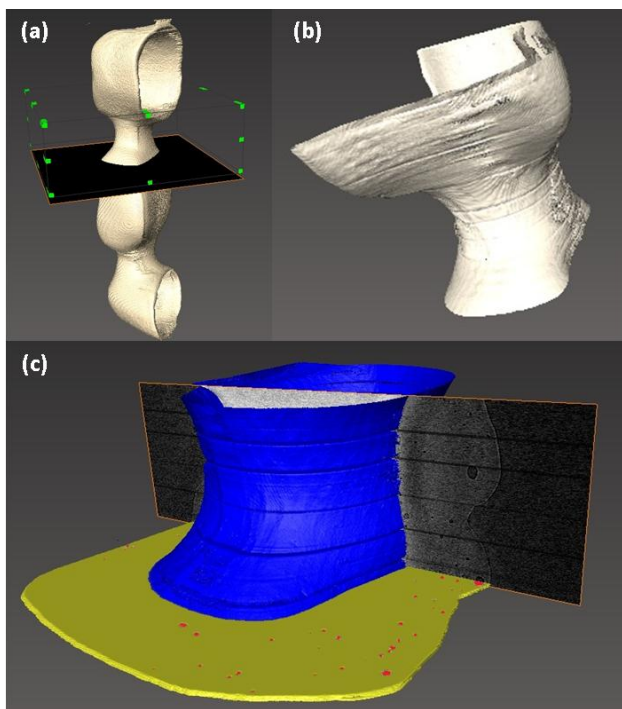


Fig. 12: 3D data rendering on (a) Zi (zirconia) dental bridge (FPD) sample using Avizo® for HEX-lab data, (b) equivalent region of the Zi part of the bridge from DLS data and (c) Zi Teeth bridge sample veneered with porcelain for DLS I12 data. Blue colour represents the Zi core, yellow represents the porcelain veneer on an arbitrary cross-section and red represent the air inclusion cloud within the porcelain due to the manufacturing process.

shows a segmented part of the porcelain-coated FPD. The zirconia part is highlighted in blue, while the porcelain veneer in an arbitrary cross-section is shown in yellow. The greyscale is used for the vertical slice through the FPD. The tomography set collected revealed a significant number of multi-sized air inclusions due the thermo-mechanical manufacturing process that could significantly affect the mechanical properties as well as the life expectancy of the prosthetic denture. The non-destructive character of X-rays combined with the high resolution tomographic imaging is very convenient for evaluating the internal structure for a variety of bulk specimens and revealing design or fabrication route deficiencies.

Using the principle of absorption tomography, it is also possible to develop “rich” tomography techniques that can then be employed to reconstruct the distribution of different kinds of physical parameters (including vectors and tensors) within sample cross-sections. The reconstruction of strain distributions uses the principles of Diffraction Strain Tomography (DST). The relative (mis)orientation maps within individual grains are obtained using Laue Orientation Tomography (LOT). These are two novel techniques developed in the HEX-lab at Oxford.

The Diffraction Strain Tomography (DST) approach [11, 12] makes use of the classical tomographic reconstruction methods, conventionally applied in the context of absorption contrast imaging, in order to obtain two-dimensional strain maps of unknown strain distributions within cross-sections of arbitrarily shaped samples under various loading conditions. A multiple-angle set of projections of the same object is collected using a diffraction setup giving information about the interplanar crystal lattice spacing distributions (average strain distribution) across the sample.

Laue Orientation Tomography (LOT) is a technique that uses the translate-rotate [11, 12] experimental procedure to obtain multiple (mis)orientation angle distribution sinograms for each of the grains found within the slice. Each sinogram represents a 2D plot of the relative lattice (mis)orientation within arbitrarily-shaped grain cross-sections in the bulk of the sample. To collect this information, Laue diffraction setup is employed, making use of polychromatic (white) X-ray beam setup to illuminate a polycrystalline sample and generate distinct Laue spots on the detector in accordance with the individual grain’s lattice orientations. Different crystal structures encountered within the illuminated volume can be distinguished in this method, so that crystallographic phase-specific analysis can be performed.

#### IV. CONCLUSIONS

X-ray texture analysis and imaging studies in the Oxford HEX-lab have been presented and reviewed. Debye-Scherrer scattering patterns obtained at the synchrotron beamline I12 at DLS were interpreted so as to obtain the ODF, and then to re-plot several key pole figures for a tungsten wire. The pole figure for the polycrystal Young’s modulus was also constructed.

X-ray tomography studies of the internal structure and defects using laboratory and synchrotron X-ray beams are also presented and discussed.

#### REFERENCES

- [1] Kocks, U.F., C.N. Tomé, and H.R. Wenk, *Texture and anisotropy: Preferred orientations in polycrystals and their effect on materials properties 1998*, Cambridge: Cambridge University Press.
- [2] Korsunsky, A.M., K.E. Wells, and P.J. Withers, *Mapping two-dimensional state of strain using synchrotron X-ray diffraction. Scripta Materialia*, 1998. 39(12): pp. 1705-1712.
- [3] Wenk, H.R. and S. Grigull, Synchrotron texture analysis with area detectors. *Journal of Applied Crystallography*, 2003. 36: pp. 1040-1049.
- [4] Hielscher, R. and H. Schaeben, A novel pole figure inversion method: specification of the MTEX algorithm. *Journal of Applied Crystallography*, 2008. 41(6): pp. 1024-1037.
- [5] Zhou, L. and S. Zhu, Development of a strain induced planar film texture as revealed by molecular dynamics simulation. *Scripta Materialia*, 2002. 47(10): pp. 677-682.
- [6] Raue, L and Klein, Calculation of anisotropic properties of dental enamel from synchrotron data. *Journal of synchrotron radiation 2011*. 18, 550-556
- [7] Zener, C., *Elasticity and anelasticity of metals 1948*, Chicago: University of Chicago Press.
- [8] Kak, A.C. and Slaney M. Principles of computerized tomographic imaging, 1988: IEEE Press.
- [9] Berger, M.J., Hubbell, J. H., Seltzer, S. M., Coursey, J. S. & Zucker, D. S., XCOM: Photon Cross Section Database 1.2, available online at <http://physics.nist.gov/xcom>, 1999.
- [10] Bay, B., et al., Digital volume correlation: Three-dimensional strain mapping using X-ray tomography. *Experimental Mechanics*, 1999. 39(3): pp. 217-226.
- [11] Korsunsky, A.M., et al., The principle of strain reconstruction tomography: Determination of quench strain distribution from diffraction measurements. *Acta Materialia*, 2006. 54(8): pp. 2101-2108.
- [12] Korsunsky, A.M., et al., Strain tomography of polycrystalline zirconia dental prostheses by synchrotron X-ray diffraction. *Acta Materialia*, 2011. 59(6): pp. 2501-2513.